

Modeling Diffusion and Permeation Across the Stratum Corneum Lipid Barrier

Rinto Thomas,^{†,¶} Praveen Ranganath Prabhakar,^{‡,¶} Douglas J. Tobias,[‡] and Michael von Domaros^{*,†}

[†]*Fachbereich Chemie, Philipps-Universität Marburg, 35032 Marburg, Germany*

[‡]*Department of Chemistry, University of California, Irvine, Irvine, California, 92697 United States*

[¶]*R.T. and P.R.P. contributed equally to this work.*

E-mail: mvondomaros@uni-marburg.de

Abstract

Human skin oils are a major sink for ozone in densely occupied indoor environments. Understanding how the resulting volatile and semivolatile organic oxidation products influence indoor air chemistry requires accurate representations not only of their emission into indoor air but also of their transport across the outermost skin barrier, the stratum corneum. Using molecular dynamics simulations, we investigate the passive permeation of acetone, 6-methyl-5-hepten-2-one, and water—two representative products of skin-oil oxidation and a reference compound—through a model stratum corneum lipid membrane. We determine position-dependent diffusivities using two complementary analyses based on the same set of simulations and evaluate their accuracy through a propagator analysis. The two approaches provide upper and lower bounds for the true diffusivity, which, when combined with previously reported free-energy profiles, yield permeabilities relevant for modeling macroscopic skin transport. Our results show that permeation is governed primarily by energetic barriers rather than by molecular mobility, and that the predicted transport coefficients vary by about one order of magnitude depending on the chosen diffusivity estimator. These findings provide molecular-level constraints for parameters used in indoor

air chemistry models and establish a transferable framework for linking atomistic transport mechanisms to large-scale simulations of human exposure and indoor air quality.

Introduction

In 2024, the mean global near-surface temperature exceeded the pre-industrial average by more than 1.5 K,¹ underscoring the increasingly tangible impacts of global warming on human health, behavior, and daily life.²⁻⁴ A plausible behavioral response—particularly among vulnerable populations such as older adults and individuals with pre-existing health conditions—is to spend more time indoors to mitigate thermal discomfort during periods of extreme heat. However, empirical evidence remains limited regarding how climate change is reshaping patterns of time use.^{5,6}

Nevertheless, because humans spend most of their time indoors, the impacts of climate change are largely mediated through indoor environments.^{7,8} Accordingly, understanding how rising outdoor temperatures influence indoor air quality has become an increasingly important research priority.^{9,10} Models and simulations are expected to play a central role in evaluating the long-term effects of climate change on indoor environments.^{11,12} However, these modeling efforts

rely on accurate physicochemical representations of the complex surface–air chemistry occurring indoors.¹³

In this study, we address this challenge by investigating the permeation of two representative volatile and semivolatile organic compounds (VOCs) through human skin. The compounds of interest—acetone and 6-MHO (Figure 1)—are formed during the ozonolysis of skin lipids, which act as the dominant ozone scavengers in densely occupied indoor environments and thus constitute an important source of secondary indoor pollutants.^{14,15} Kinetic models have been developed to describe the mass transport and chemical transformations of these oxidation products across the skin, surrounding air, and clothing.^{16,17} However, the reliability of such models depends critically on accurate physicochemical parameters describing the partitioning of semivolatile compounds—such as 6-MHO—between the human body and indoor air,¹⁸ as well as on reliable descriptions of their diffusional transport through the skin barrier.

To address this challenge, we recently began investigating permeation energetics using atomistic molecular dynamics (MD) simulations of stratum corneum (SC) lipid membranes (Fig 1)—the skin’s primary barrier to chemical penetration.¹⁹ We found that the convergence of free-energy (FE) profiles describing the translocation of permeants across these membranes was remarkably slow, requiring microseconds of simulation time even when state-of-the-art enhanced sampling techniques were employed. We traced the molecular origin of this convergence bottleneck to the highly ordered structure of SC membranes, which contrasts sharply with the fluid-like organization of conventional lipid bilayers such as those composed of 1-palmitoyl-2-oleoyl-*sn*-glycero-3-phosphocholine (POPC). In addition, we identified stochastic lipid flip–flop events between the two membrane leaflets that induce long-lived structural asymmetries.

In this work, we extend our previous investigations by providing estimates of diffusivity profiles along the membrane normal. Predicting these diffusivities remains a challenging task—particularly when permeation is slow and enhanced sampling is required to overcome large

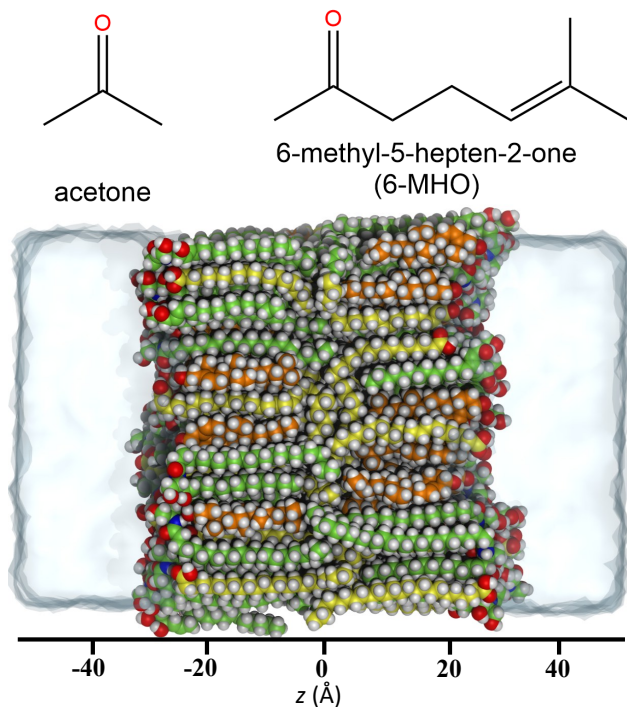


Figure 1: Chemical structures of acetone and 6-MHO, and a representative snapshot of the model system. The atomistic lipid membrane is composed of cholesterol (orange), lignoceric acid (yellow), and ceramide NS (green). In this study, we investigate solute permeation across the membrane along the z -axis. Figure adapted with permission from ref.¹⁹.

FE barriers. We employ two complementary approaches to compute position-dependent diffusivities from harmonically restrained MD simulations, based on either the velocity autocorrelation function (VACF)²⁰ or the position autocorrelation function (PACF)²¹ of the coordinate describing membrane permeation. As shown by our results—and consistent with the findings of Rowley *et al.* for a dipalmitoylphosphatidylcholine (DPPC) membrane²²—estimates obtained from the two approaches differ substantially. Through a rigorous propagator-based analysis, we demonstrate that the resulting diffusivity profiles provide lower and upper bounds to the true profile. We further propagate these results to obtain single-membrane permeabilities and we critically assess how methodological uncertainties affect the accuracy of these predictions. Taken together, our work advances the understanding of molecular permeation across skin lipid membranes and establishes a robust framework for improving predictive models of indoor air chemistry under changing environmental conditions.

Methods

The model systems and simulation protocol have been described in detail in our previous study.¹⁹ Here, we briefly summarize the main aspects relevant to the present work and describe the computation of position-dependent diffusivities and the propagator analysis.

Model Systems

We studied three solutes—acetone, 6-MHO, and water—representing two skin-oil oxidation products and a reference compound. These solutes permeate through a model stratum corneum (SC) lipid bilayer, originally proposed by Klauda *et al.*, and representative of the short periodicity phase (SPP)—the tightly packed lamellar arrangement of lipids that forms the primary diffusion barrier in the SC (Figure 1).^{23,24}

Umbrella Sampling

The translocation of the solutes across the membrane is described by a collective variable (CV), denoted as z , which measures the center-of-mass distance between each solute and the membrane projected onto the membrane normal (Figure 1).

For each solute, we performed 91 independent simulations (windows), in which the solute was harmonically restrained at integer-Å positions along the z coordinate (umbrella sampling, US). A detailed analysis of the influence of the harmonic force constant was presented by Rowley *et al.*,²² and our own related findings on this topic are provided in Section S1 of the Supporting Information (SI). For the results reported in the main text, a force constant of $30 \text{ kcal mol}^{-1} \text{ \AA}^{-2}$ is employed. Each simulation is initiated from well-equilibrated configurations obtained in our previous study and run for 15 ns per window.

All simulations are conducted at the physiological skin temperature of $T = 305.15 \text{ K}$, maintained by a stochastic velocity-rescaling thermostat²⁵ with a time constant of 1 ps, and performed using NAMD 3.0 (alpha13).^{26,27}

Diffusivity Profiles

Two approaches are used to compute the position-dependent diffusivities, $D(z)$, along the membrane normal.

The first approach, proposed by Woolf and Roux, relies on the calculation of the velocity autocorrelation function (VACF):²⁰

$$C_v(t) = \langle \dot{z}(t)\dot{z}(0) \rangle, \quad (1)$$

followed by the evaluation of a Laplace-frequency-dependent diffusivity,

$$D(s) = \frac{-\hat{C}_v(s) \langle \delta z^2 \rangle \langle \dot{z}^2 \rangle}{\hat{C}_v(s)[s\langle \delta z^2 \rangle + s^{-1}\langle \dot{z}^2 \rangle] - \langle \delta z^2 \rangle \langle \dot{z}^2 \rangle}, \quad (2)$$

where $\hat{C}_v(s)$ denotes the Laplace transform of $C_v(t)$. The local diffusion coefficient is then obtained in the limit

$$D(z = \langle z \rangle) = \lim_{s \rightarrow 0} D(s), \quad (3)$$

which, however, is mathematically ill-defined and therefore requires an empirical extrapolation procedure.

Hummer later proposed an alternative approach that avoids Laplace-domain extrapolation by using the position autocorrelation function (PACF):²¹

$$C_{\delta z}(t) = \frac{\langle \delta z(t) \delta z(0) \rangle}{\langle \delta z^2 \rangle}, \quad (4)$$

$$D(z = \langle z \rangle) = \frac{\langle \delta z^2 \rangle}{\int_0^\infty C_{\delta z}(t) dt}. \quad (5)$$

In practice, however, one must either impose a cutoff time for the integral or assume a functional form to fit the correlation decay—both of which can introduce systematic bias.

The velocities required for computing the VACF are obtained from finite differences of the CV trajectory, which is saved at 2 fs intervals. Position-dependent diffusivities are determined using the ACFCalculator code developed by Rowley *et al.*, which implements a heuristic procedure for the extrapolation in eq. 3.²²

We note that alternative strategies for estimating position-dependent diffusivities are available. In particular, Bayesian-inference methods were originally proposed by Hummer²⁸ and later extended to anisotropic media by Ghysels *et al.*²⁹ They have also been coupled to adaptive biasing force calculations by Comer, Chipot, and co-workers.^{30,31} Complementary formulations have been developed by Rosta and collaborators.^{32,33} We focus here on the VACF/PACF approaches because they are widely used in membrane-permeation studies,^{34–38} straightforward to implement on the same umbrella-sampling data, and allow direct comparison to prior results for our benchmark system (water).

Propagator Analysis

Diffusion in inhomogeneous media can be described by the Smoluchowski equation. In the one-dimensional case relevant to this study, the position- and time-dependent probability den-

sity $p(z, t)$ evolves according to

$$\partial_t p(z, t) = \partial_z \left\{ D(z) e^{-\beta \Delta F(z)} \partial_z \left[e^{\beta \Delta F(z)} p(z, t) \right] \right\}, \quad (6)$$

where $\beta = 1/(k_B T)$ is the inverse thermal energy, $\Delta F(z)$ denotes the FE profile, and $D(z)$ represents the position-dependent diffusivity.

For given $\Delta F(z)$ and $D(z)$ profiles and a delta-function initial condition, $p(z, t_0) = \delta(z - z_0)$, this equation can be solved numerically using a standard forward-in-time, centered-in-space (FTCS) finite-difference scheme. The resulting solution, $p(z, t | z_0, t_0)$, represents the propagator of the diffusion model—that is, the conditional probability of finding a particle initially located at $z(t_0) = z_0$ at position $z(t)$ at a later time t . The same quantity can also be obtained directly from molecular dynamics (MD) simulations without assuming diffusive behavior, thereby providing a rigorous test of the accuracy of the proposed $\Delta F(z)$ and $D(z)$ profiles.

We compute MD-derived propagators for the critical membrane-core region as follows. A total of 1800 snapshots were selected in which the solute was located near the membrane center ($|z| < 0.05 \text{ \AA}$). The harmonic restraint was then removed, allowing the solute to freely explore the entire membrane. Unrestrained simulations were run for 15 ns, and propagators $p(z, t | z_0 = 0, t_0 = 0)$ for selected lag times t were estimated from histograms along the z coordinate.

Results and Discussion

Diffusivity Profiles

Diffusivity profiles, $D(z)$, of the solutes along the transmembrane axis were estimated from the same set of simulations using the PACF and VACF approaches described above. The resulting profiles are shown in Figure 2.

For all three systems, the PACF method yields constant diffusivities in the aqueous regions ($|z| > 40 \text{ \AA}$) surrounding the membrane, which agree well with the corresponding bulk-phase diffusivities obtained from separate simulations (Section S2). The VACF method produces comparable results in this region for acetone and

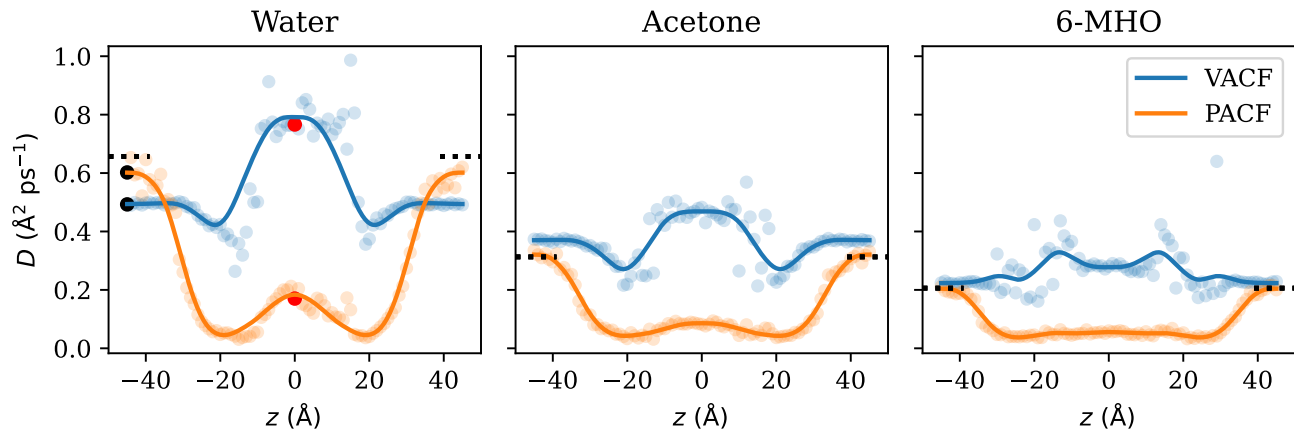


Figure 2: Transmembrane diffusivity profiles obtained from the velocity autocorrelation function (VACF) and position autocorrelation function (PACF) analyses. Quantitative and qualitative discrepancies are evident near the membrane center. Solid lines are shown to guide the eye, and dashed lines indicate reference values for the aqueous-phase bulk diffusivities. In the water profile, two representative data points—one in the bulk region (black) and one at the membrane center (red)—are highlighted for further analysis.

6-MHO but deviates by approximately 24 % for water.

In the headgroup region, both methods indicate a local diffusivity bottleneck for all solutes. The most pronounced discrepancy between the two approaches, however, appears at the membrane center, where the estimates differ both quantitatively and qualitatively: the VACF method predicts higher-than-bulk diffusivities, whereas the PACF method yields lower values. Similar observations were reported by Rowley *et al.* for a DPPC membrane.²² In the following, we discuss the challenges associated with determining diffusivities using both approaches and the likely origins of these discrepancies. Our analysis focuses primarily on two representative regions of the membrane: the aqueous region, where the two methods show good agreement, and the membrane center, where the discrepancies are most pronounced.

Challenge 1: Extrapolation of the VACF Results

Obtaining position-dependent diffusivities from VACFs requires computing a Laplace-frequency-dependent diffusivity, $D(s)$, for each US window (eq. 2), followed by extrapolation

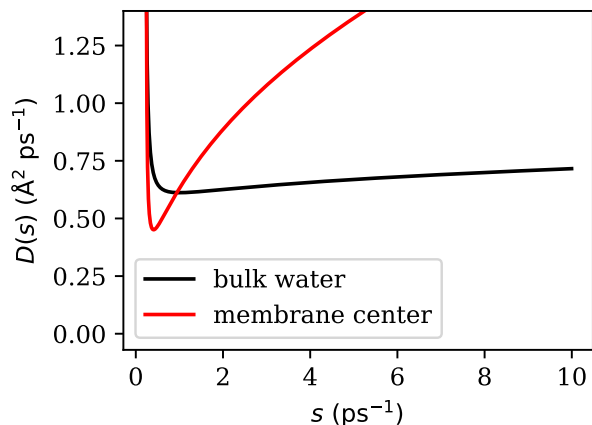


Figure 3: Illustration of determining diffusivities from velocity autocorrelation functions. The quantity $D(s)$, computed from eq. 2, must be extrapolated to zero by fitting a straight line over a range of s values where the function remains well-behaved. This procedure performs reliably in the bulk phase but is highly sensitive to the placement of the tangent line for windows at the membrane center. The values obtained using the automated extrapolation procedure of Rowley *et al.*²² are indicated by the black and red points in Figure 2.

to zero frequency (eq. 3). However, this limit is ill-defined because of the s^{-1} dependence of $D(s)$ and therefore necessitates an empirical extrapolation procedure. Our VACF-based diffusivity profiles were obtained using the automated linear extrapolation method of Rowley *et al.*²² Although this approach is relatively robust in the aqueous bulk region, it may not be optimal at the membrane center (Figure 3). Because $D(s)$ exhibits pronounced curvature in the membrane core, the linear extrapolation is highly sensitive to the placement of the tangent line, yielding diffusivity estimates between roughly $0.1 \text{ \AA}^2/\text{ps}$ and $0.75 \text{ \AA}^2/\text{ps}$.

Challenge 2: Determination of PACF Correlation Times

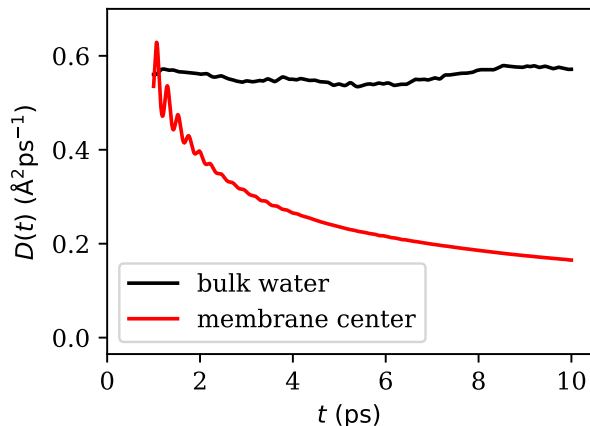


Figure 4: Illustration of determining diffusivities from position autocorrelation functions (PACFs). Shown is the estimated diffusivity, $D(t)$, as a function of the PACF integration cutoff time in two selected regions of the membrane. In the absence of noise, $D(t)$ should reach a plateau. A clear plateau is visible in the bulk water region but not at the membrane center. The values corresponding to a fixed cutoff of $t = 10$ ps are indicated by the black and red points in Figure 2.

The challenges associated with extrapolating $D(s)$ to zero frequency were recognized by Hummer, who proposed an alternative approach based on determining the PACF correlation time (eq. 5).²⁸ For purely diffusive dynamics, this

method is formally equivalent to the VACF approach, but it is considerably simpler to apply in practice.

In Figure 4, we show selected diffusivities, $D(t)$, as a function of the integration cutoff time used in eq. 5. The PACF method performs well when the solute resides in the aqueous phase, where $D(t)$ reaches a clear plateau between approximately 8 ps and 10 ps. Although noise leads to some fluctuations, it does not significantly alter the predicted diffusivity. In contrast, at the membrane center, the decay of the PACF is substantially slower, and no clear plateau in $D(t)$ is observed even after 10 ps. These observations are consistent with those reported by Rowley *et al.* for a DPPC membrane.²²

As a consequence, solute- and region-specific integration cutoffs would be ideal but require tedious manual adjustment. Instead, the diffusivity profiles in Figure 2 were obtained using practical compromise cutoffs: 8 ps for water and 10 ps for acetone and 6-MHO. Although these fixed cutoffs may slightly overestimate PACF-derived diffusivities in certain regions (e.g., the membrane center), our main conclusions are unaffected: PACF-derived profiles still represent lower bounds to the true $D(z)$.

Propagator Analysis

Having obtained two qualitatively distinct diffusivity profiles from the same set of simulations, it is natural to ask which of the two, if either, is correct. To address this question, we computed the propagators of both diffusion models in the critical membrane-center region, $p(z, t | z_0 = 0, t_0 = 0)$ —that is, the probability of finding a particle initially located at $z_0 = 0$ at position z after a lag time t . The corresponding FE profiles were taken from our previous study,¹⁹ as shown in Figure 5. For the present analysis, we used the umbrella-sampling (US)-based free-energy profiles. A comparison between the model-derived propagators and those obtained directly from molecular dynamics simulations is presented in Figure 6 for two representative lag times.

At short lag times ($t = 2$ ps), the VACF-based model shows quantitative agreement with the

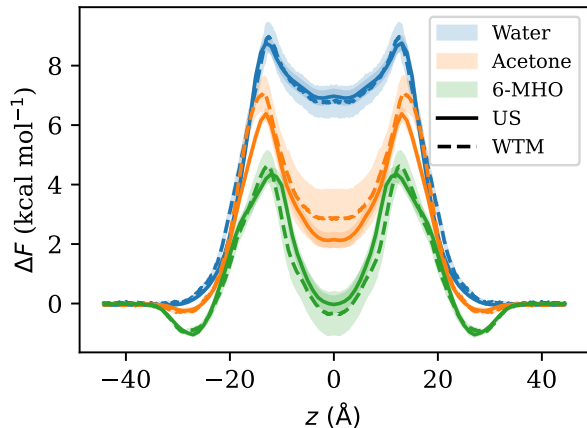


Figure 5: Free-energy profiles for the translocation of all solutes across the model stratum corneum membrane, obtained from umbrella sampling (US) and well-tempered metadynamics (WTM).¹⁹ The two methods produce consistent overall features, with only minor quantitative differences. Figure adapted with permission from ref.¹⁹.

simulation data over six orders of magnitude, whereas the PACF approach fails to do so. This finding is consistent with the results reported by Rowley *et al.*,²² who performed a simplified analysis by approximating the propagator as a normal distribution—an assumption that holds only for lag times long enough to reproduce diffusive dynamics yet short enough that the effects of inhomogeneity remain negligible.

However, it is not obvious that the lag time of 2 ps chosen here (or the 5 ps used by Rowley *et al.*) is sufficiently long for the diffusive approximation to hold. Indeed, the failure of the PACF to decay within such short timescales may also be interpreted as a breakdown of this assumption. Subdiffusive behavior has, in fact, been reported for lag times up to at least 64 ps for methanol permeation across a POPC membrane.³¹

We therefore extended our propagator analysis to selected lag times of up to 500 ps. For a range of lag times between 50 ps and 500 ps, which we consider to lie within the truly diffusive regime, the model propagators exhibit the behavior shown for the representative case of $t = 100$ ps in Figure 6. The complete set of

results is provided in Section S3.

At these timescales, neither the VACF- nor the PACF-based models reproduce the simulation data quantitatively. However, the VACF results consistently overestimate the diffusive spread (i.e., the diffusivities are too large), whereas the PACF results underestimate it (i.e., the diffusivities are too small). We therefore interpret the two profiles as providing upper and lower bounds, respectively, to the true diffusivity profile, which must lie between them. In the following, these bounds are used to assess the sensitivity of derived quantities, specifically the transmembrane permeabilities.

Impact on Permeabilities

Within the inhomogeneous solubility–diffusion (ISD) model,^{39,40} the local resistance of a membrane to permeation, $R(z)$, is expressed in terms of the diffusivity and FE profiles as

$$R(z) = \frac{e^{\beta\Delta F(z)}}{D(z)}. \quad (7)$$

The overall permeability of the membrane, P , is then obtained by integrating the resistance over the membrane width, h , according to

$$\frac{1}{P} = \int_{-h/2}^{+h/2} R(z) dz. \quad (8)$$

Using the FE profiles for the translocation of all solutes across the membrane (Figure 5), we computed the membrane permeabilities according to eqs 7 and 8. The resulting permeabilities are shown in Figure 7, and the corresponding numerical values are provided in the Supporting Information (Section S4). Because of the exponential dependence on the free energy in eq 7, even small variations in $\Delta F(z)$ are amplified, leading to pronounced differences in the resulting permeabilities, which follow the order 6-MHO > acetone \gg water.

We have also shown that the FE profiles obtained from US and WTM differ slightly (Figure 5), even after extensive sampling, although these differences remain within the limits of statistical uncertainty.¹⁹ With the diffusivity profiles now available, we can propagate the

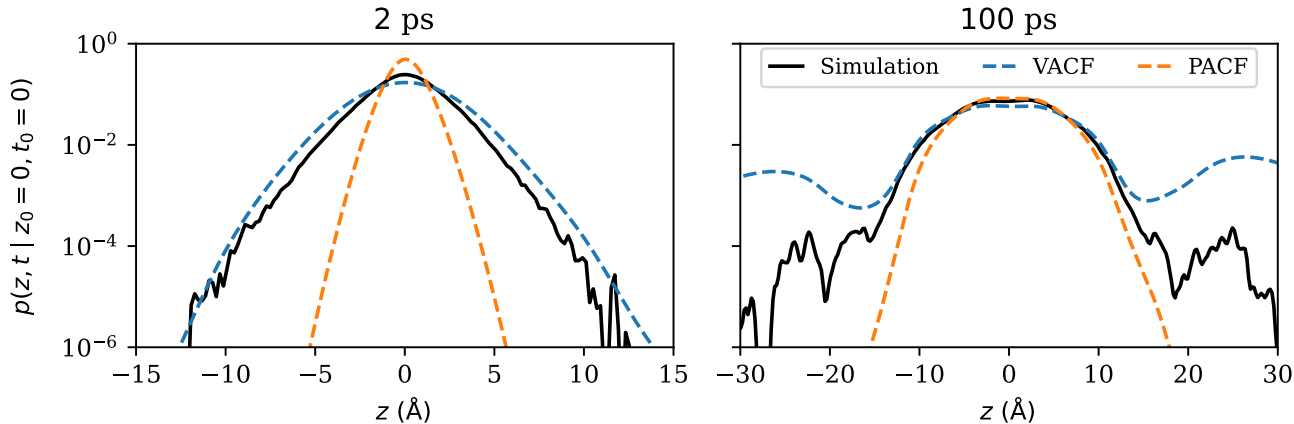


Figure 6: Propagators, $p(z, t | z_0, t_0)$, representing the probability of finding a particle initially located at $z_0 = 0$ at position z after a lag time t . Shown are results obtained by numerically solving the Smoluchowski diffusion equation using diffusivity profiles derived from the velocity autocorrelation function (VACF) and position autocorrelation function (PACF) analyses, compared with direct simulation data. At short lag times ($t = 2$ ps), the VACF-based model shows quantitative agreement with the simulation data, although the true diffusive regime has likely not yet been reached on this timescale. At longer lag times ($t = 100$ ps), the VACF- and PACF-based models provide upper and lower bounds, respectively, to the true propagators and, by extension, to the diffusivity profile.

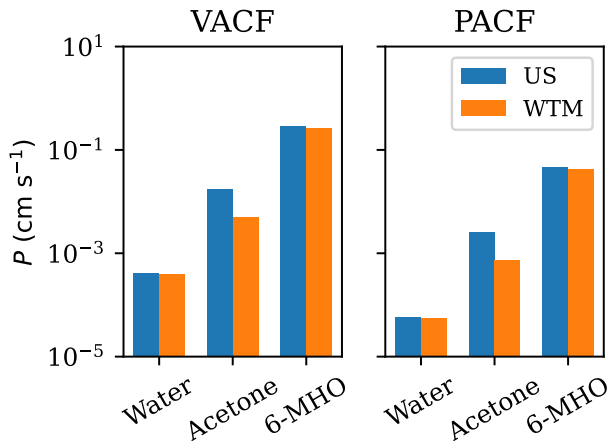


Figure 7: Membrane permeabilities estimated using diffusivity profiles derived from the velocity autocorrelation function (VACF, left) and position autocorrelation function (PACF, right) analyses, each combined with free-energy profiles obtained from umbrella sampling (US) and well-tempered metadynamics (WTM). Differences between the free-energy methods are noticeable only for acetone, whereas discrepancies between the two diffusivity analyses consistently span approximately one order of magnitude across all solutes.

different FE profiles to evaluate their impact on the resulting transport coefficients. We find good agreement between the results obtained from both methods for water and 6-MHO; for acetone, however, noticeable deviations are observed. Nevertheless, the permeability coefficients for all solutes differ by less than an order of magnitude, indicating that statistical variations between FE methods likely have little to no impact on kinetic model predictions.

More striking are the differences in permeabilities when comparing VACF- and PACF-derived diffusivities. Because the VACF-derived diffusivities are consistently higher than those obtained from the PACF method, the same trend is reflected in the corresponding permeabilities. In absolute terms, deviations reach approximately one order of magnitude. Whether such differences are significant for kinetic models is highly problem specific. In many cases, these discrepancies are likely acceptable, although the final assessment should be guided by a dedicated sensitivity analysis.¹⁷

Finally, we examined the influence of the integration limits used in eq. 8. Typically, h is defined as the full thickness of the membrane. How-

ever, for heterogeneous, multicomponent lipid membranes such as the SC system investigated here, determining precise interfacial boundaries ($\pm h/2$) is nontrivial. We therefore considered three plausible definitions for $h/2$, based on the membrane density profile (Section S4): (i) the position where the water density begins to decrease from its bulk value ($h_1/2 = 32.0 \text{ \AA}$); (ii) the position where the water density is reduced to half of its bulk value ($h_2/2 = 25.5 \text{ \AA}$); and (iii) the position where the water density approaches zero ($h_3/2 = 17.0 \text{ \AA}$).

To investigate the impact of these definitions, we show the local resistance $R(z)$ in Figure 8. The area under each curve corresponds to the inverse permeability, P^{-1} . Within the membrane interior, this area is several orders of magnitude larger than the small additional contributions from the interfacial regions. We therefore conclude that different reasonable integration limits have little to no effect on the computed permeabilities.

Conclusions

We used MD simulations to quantify position-dependent diffusivities, $D(z)$, for water, acetone, and 6-MHO across a representative SC lipid membrane and combined these results with previously reported FE profiles to compute transmembrane permeabilities, P . By applying both PACF- and VACF-based analyses to the same set of US trajectories and validating them through a propagator comparison, we demonstrated that the two $D(z)$ estimates systematically bracket the true diffusivity profile in the diffusive regime, with PACF providing a lower bound and VACF an upper bound. Permeabilities derived from these bounds consequently span approximately one order of magnitude, whereas differences arising from the choice of FE method (US vs. WTM) become negligible once propagated to transport parameters. Consistent with the exponential dependence of the ISD framework on free energy, the ordering of permeabilities follows the underlying FE landscape rather than the local diffusivities—6-MHO $>$ acetone \gg water—highlighting that permeation

across the membrane is governed primarily by energetic barriers rather than by differences in molecular mobility.

Direct comparison of permeabilities computed from our MD simulations to experimental values (in vitro^{41,42} or in vivo⁴³) is not straightforward because our model represents a simplified SC membrane composed of an equimolar mixture of ceramides, free fatty acids, and cholesterol. In contrast, native human SC exhibits substantial lipid heterogeneity, encompassing a broad spectrum of ceramide subclasses and chain-length distributions.⁴⁴ Nevertheless, the water permeability obtained using PACF-derived diffusivities is within the same order of magnitude as the experimental estimate of Gupta *et al.* ($7.08 \pm 1.18 \times 10^{-5} \text{ cm s}^{-1}$),³⁵ with residual differences most likely reflecting variations between the GROMOS and CHARMM force fields.

Permeability coefficients are often estimated empirically using quantitative structure–activity relationship (QSAR) and continuum diffusion models,^{45–49} which correlate measured permeabilities with molecular descriptors such as molar mass, partition coefficients, and bulk diffusion constants. Although such models are powerful for interpolation within their training domains, they do not explicitly capture the molecular-scale interactions and dynamic heterogeneity that govern transport across the SC lipid matrix—especially when applied to molecules that fall outside their original parameterization range. In contrast, MD simulations capture these effects directly by resolving how solutes interact with and move through the heterogeneous lipid environment. For example, despite its larger molar mass relative to water and acetone, 6-MHO exhibits the highest permeability because of its comparatively low free-energy barriers to permeation (Figure 5), underscoring the dominant role of thermodynamic driving forces—rather than molecular size—in determining SC transport.

With respect to indoor air chemistry, several kinetic models—such as KM-BL, KM-FILM, and KM-SUB-Skin-Clothing¹⁷—have been developed to describe the dynamics of skin-oil oxidation products across different interfaces. However, these models critically depend on physic-

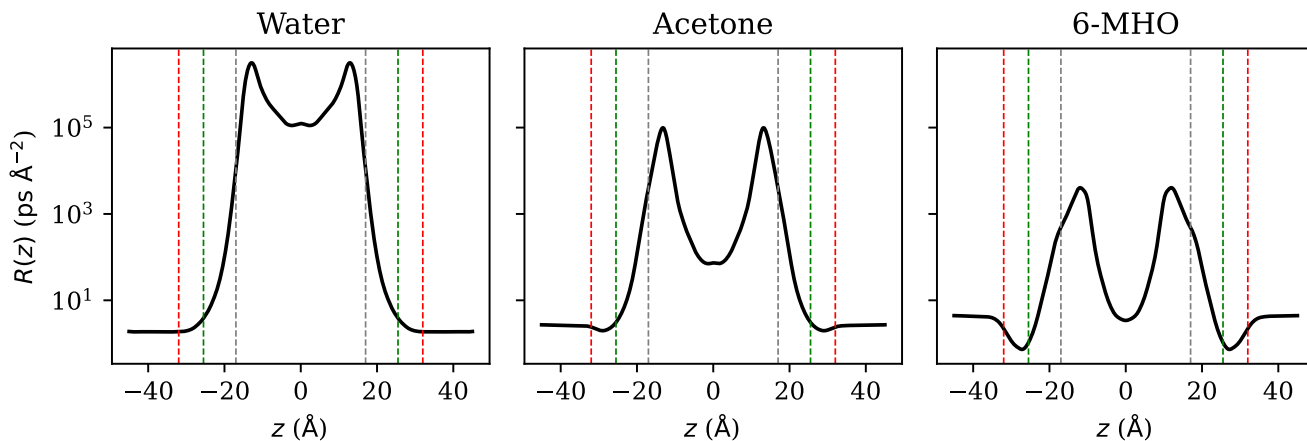


Figure 8: Local resistance, $R(z)$, estimated using free-energy profiles obtained from umbrella sampling and diffusivity profiles derived from the velocity autocorrelation function analysis. The corresponding results for other combinations of free-energy and diffusivity methods are provided in Section S4. The red, green, and gray vertical lines indicate different plausible integration limits. The areas under the curves in these regions are negligible compared with the contributions from the membrane center, indicating that different integration limits have little impact on the overall permeability.

ochemical parameters that are difficult or impossible to measure experimentally, underscoring the value of molecular-scale simulations like those presented here. For example, Lakey *et al.* demonstrated that the performance of their KM-FILM model is highly sensitive to the assumed diffusion constants of surface films,⁵⁰ illustrating how improved microscopic input can directly enhance macroscopic predictive accuracy.

Taken together, our results provide mechanistic and quantitative constraints—via upper and lower bounds on $D(z)$ and permeabilities—that can be directly used to refine existing indoor-air kinetic models. Beyond these applications, the present framework establishes a foundation for systematically linking atomistic transport processes to macroscopic exposure and air-quality models. Future directions include (i) extending the approach to multilamellar SC architectures and anisotropic membrane transport; (ii) assessing the influence of force-field and water-model choice; (iii) developing more robust and transferable diffusivity estimators; and (iv) performing targeted experimental validation for VOCs of indoor relevance. Collectively, these efforts will help bridge the scale gap between molecular transport and human exposure in complex indoor environments.

Acknowledgement The authors thank Chinmay Das and Peter D. Olmsted for helpful discussions on setting up SC models. DJT acknowledges support from the Alfred P. Sloan Foundation Chemistry of the Indoor Environment (CIE) Program (G-2020-13912).

Supporting Information Available

The supporting information includes an assessment of the influence of the harmonic force constant on diffusivity profiles; details on the calculation of bulk diffusivities from mean-squared displacements; the complete set of propagator analyses across different lag times; density profiles used to define membrane boundaries; additional local resistance profiles obtained from all combinations of free-energy and diffusivity methods; and a table summarizing all computed permeability coefficients.

References

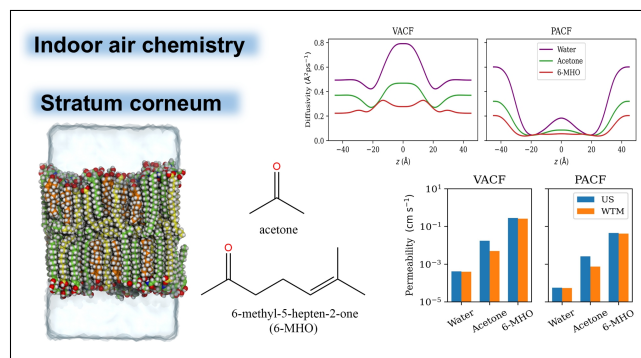
- (1) World Meteorological Organization (WMO) *State of the Global Climate 2024*;

- 2025.
- (2) Rocque, R. J.; Beaudoin, C.; Ndjaboue, R.; Cameron, L.; Poirier-Bergeron, L.; Poulin-Rheault, R.-A.; Fallon, C.; Tricco, A. C.; Witteman, H. O. Health effects of climate change: An overview of systematic reviews. *BMJ Open* **2021**, *11*, e046333.
 - (3) Intergovernmental Panel on Climate Change (IPCC), Ed. *Global warming of 1.5°C: IPCC special report on impacts of global warming of 1.5°C above pre-industrial levels in context of strengthening response to climate change, sustainable development, and efforts to eradicate poverty*; Cambridge University Press: Cambridge, 2022; pp 175–312.
 - (4) Abdul-Nabi, S. S.; Karaki, V. A.; Khalil, A.; Zahran, T. E. Climate change and its environmental and health effects from 2015 to 2022: A scoping review. *Heliyon* **2025**, *11*.
 - (5) White-Newsome, J. L.; Sánchez, B. N.; Jolliet, O.; Zhang, Z.; Parker, E. A.; Dvonch, J. T.; O’Neill, M. S. Climate change and health: Indoor heat exposure in vulnerable populations. *Environ. Res.* **2012**, *112*, 20–27.
 - (6) Connolly, M. Climate change and the allocation of time. *IZA World Labor* **2018**,
 - (7) Institute of Medicine *Climate change, the indoor environment, and health*; 2011.
 - (8) Spengler, J. D. Climate change, indoor environments, and health. *Indoor Air* **2012**, *22*, 89–95.
 - (9) Nazaroff, W. W. Exploring the consequences of climate change for indoor air quality. *Environ. Res. Lett.* **2013**, *8*, 015022.
 - (10) Mansouri, A.; Wei, W.; Alessandrini, J.-M.; Mandin, C.; Blondeau, P. Impact of climate change on indoor air quality: A review. *Int. J. Environ. Res. Public Health* **2022**, *19*, 15616.
 - (11) Zhao, J.; Uhde, E.; Salthammer, T.; Antretter, F.; Shaw, D.; Carslaw, N.; Schieweck, A. Long-term prediction of the effects of climate change on indoor climate and air quality. *Environ. Res.* **2024**, *243*, 117804.
 - (12) Zhao, J.; Salthammer, T.; Schieweck, A.; Uhde, E.; Hussein, T. Long-term prediction of climate change impacts on indoor particle pollution: Case study of a residential building in Germany. *Environ. Sci.: Processes Impacts* **2025**, *27*, 1688–1703.
 - (13) von Domaros, M.; Tobias, D. J. Molecular dynamics simulations of the interactions of organic compounds at indoor-relevant surfaces. *Annu. Rev. Phys. Chem.* **2025**, *76*, 231–250.
 - (14) Wisthaler, A.; Weschler, C. J. Reactions of ozone with human skin lipids: Sources of carbonyls, dicarbonyls, and hydroxycarbonyls in indoor air. *Proc. Natl. Acad. Sci. U.S.A.* **2010**, *107*, 6568–6575.
 - (15) Weschler, C. J. Roles of the human occupant in indoor chemistry. *Indoor Air* **2016**, *26*, 6–24.
 - (16) Lakey, P. S. J.; Wisthaler, A.; Berke-meier, T.; Mikoviny, T.; Pöschl, U.; Shiraiwa, M. Chemical kinetics of multiphase reactions between ozone and human skin lipids: Implications for indoor air quality and health effects. *Indoor Air* **2017**, *27*, 816–828.
 - (17) Lakey, P. S. J.; Morrison, G. C.; Won, Y.; Parry, K. M.; von Domaros, M.; Tobias, D. J.; Rim, D.; Shiraiwa, M. The impact of clothing on ozone and squalene ozonolysis products in indoor environments. *Commun. Chem.* **2019**, *2*, 1–8.
 - (18) von Domaros, M.; Lakey, P. S. J.; Shiraiwa, M.; Tobias, D. J. Multiscale modeling of human skin oil-induced indoor air chemistry: Combining kinetic models and molecular dynamics. *J. Phys. Chem. B* **2020**, *124*, 3836–3843.

- (19) Thomas, R.; Prabhakar, P. R.; Tobias, D. J.; von Demaros, M. Insights into dermal permeation of skin oil oxidation products from enhanced sampling molecular dynamics simulation. *J. Phys. Chem. B* **2025**, *129*, 1784–1794.
- (20) Woolf, T. B.; Roux, B. Conformational flexibility of *O*-phosphorylcholine and *o*-phosphorylethanolamine: A molecular dynamics study of solvation effects. *J. Am. Chem. Soc.* **1994**, *116*, 5916–5926.
- (21) Hummer, G. Position-dependent diffusion coefficients and free energies from Bayesian analysis of equilibrium and replica molecular dynamics simulations. *New J. Phys.* **2005**, *7*, 34.
- (22) Gaalswyk, K.; Awoonor-Williams, E.; Rowley, C. N. Generalized Langevin methods for calculating transmembrane diffusivity. *J. Chem. Theory Comput.* **2016**, *12*, 5609–5619.
- (23) Das, C.; Olmsted, P. D. The physics of stratum corneum lipid membranes. *Philos. Trans. R. Soc., A* **2016**, *374*, 20150126.
- (24) Wang, E.; Klauda, J. B. Models for the stratum corneum lipid matrix: Effects of ceramide concentration, ceramide hydroxylation, and free fatty acid protonation. *J. Phys. Chem. B* **2018**, *122*, 11996–12008.
- (25) Bussi, G.; Donadio, D.; Parrinello, M. Canonical sampling through velocity rescaling. *J. Chem. Phys.* **2007**, *126*, 014101.
- (26) Phillips, J. C.; Braun, R.; Wang, W.; Gumbart, J.; Tajkhorshid, E.; Villa, E.; Chipot, C.; Skeel, R. D.; Kalé, L.; Schulten, K. Scalable molecular dynamics with NAMD. *J. Comput. Chem.* **2005**, *26*, 1781–1802.
- (27) Phillips, J. C. et al. Scalable molecular dynamics on CPU and GPU architectures with NAMD. *J. Chem. Phys.* **2020**, *153*, 044130.
- (28) Hummer, G. Position-dependent diffusion coefficients and free energies from Bayesian analysis of equilibrium and replica molecular dynamics simulations. *New J. Phys.* **2005**, *7*, 34.
- (29) Ghysels, A.; Venable, R. M.; Pastor, R. W.; Hummer, G. Position-dependent diffusion tensors in anisotropic media from simulation: Oxygen transport in and through membranes. *J. Chem. Theory Comput.* **2017**, *13*, 2962–2976.
- (30) Comer, J.; Chipot, C.; González-Nilo, F. D. Calculating position-dependent diffusivity in biased molecular dynamics simulations. *J. Chem. Theory Comput.* **2013**, *9*, 876–882.
- (31) Chipot, C.; Comer, J. Subdiffusion in membrane permeation of small molecules. *Sci. Rep.* **2016**, *6*, 35913.
- (32) Rosta, E.; Hummer, G. Free energies from dynamic weighted histogram analysis using unbiased Markov state models. *J. Chem. Theory Comput.* **2015**, *11*, 276–285.
- (33) Sicard, F.; Koskin, V.; Annibale, A.; Rosta, E. Position-dependent diffusion from biased simulations and Markov state model analysis. *J. Chem. Theory Comput.* **2021**, *17*, 2022–2033.
- (34) Das, C.; Olmsted, P. D.; Noro, M. G. Water permeation through stratum corneum lipid bilayers from atomistic simulations. *Soft Matter* **2009**, *5*, 4549–4555.
- (35) Gupta, R.; Sridhar, D. B.; Rai, B. Molecular dynamics simulation study of permeation of molecules through skin lipid bilayer. *J. Phys. Chem. B* **2016**, *120*, 8987–8996.
- (36) Krämer, A.; Ghysels, A.; Wang, E.; Venable, R. M.; Klauda, J. B.; Brooks, B. R.; Pastor, R. W. Membrane permeability of small molecules from unbiased molecular dynamics simulations. *J. Chem. Phys.* **2020**, *153*, 124107.

- (37) Piasentin, N.; Lian, G.; Cai, Q. Evaluation of constrained and restrained molecular dynamics simulation methods for predicting skin lipid permeability. *ACS Omega* **2021**, *6*, 35363–35374.
- (38) Reuter, M.; Joseph, E.; Lian, G.; Lunter, D. J. Presence of different ceramide species modulates barrier function and structure of stratum corneum lipid membranes: Insights from molecular dynamics simulations. *Mol. Pharm.* **2025**, *22*, 4280–4292.
- (39) Diamond, J. M.; Katz, Y. Interpretation of nonelectrolyte partition coefficients between dimyristoyl lecithin and water. *J. Membr. Biol.* **1974**, *17*, 121–154.
- (40) Marrink, S.-J.; Berendsen, H. J. C. Simulation of water transport through a lipid membrane. *J. Phys. Chem.* **1994**, *98*, 4155–4168.
- (41) Anderson, B. D.; Higuchi, W. I.; Raykar, P. V. Heterogeneity effects on permeability–partition coefficient relationships in human stratum corneum. *Pharm. Res.* **1988**, *5*, 566–573.
- (42) Anderson, B. D.; Raykar, P. V. Solute structure–permeability relationships in human stratum corneum. *J. Invest. Dermatol.* **1989**, *93*, 280–286.
- (43) Kalia, Y. N.; Pirot, F.; Guy, R. H. Homogeneous transport in a heterogeneous membrane: Water diffusion across human stratum corneum in vivo. *Biophys. J.* **1996**, *71*, 2692–2700.
- (44) van Smeden, J.; Janssens, M.; Gooris, G. S.; Bouwstra, J. A. The important role of stratum corneum lipids for the cutaneous barrier function. *Biochim. Biophys. Acta, Mol. Cell Biol. Lipids* **2014**, *1841*, 295–313.
- (45) Wilschut, A.; ten Berge, W. F.; Robinson, P. J.; McKone, T. E. Estimating skin permeation: The validation of five mathematical skin permeation models. *Chemosphere* **1995**, *30*, 1275–1296.
- (46) Lian, G.; Chen, L.; Han, L. An evaluation of mathematical models for predicting skin permeability. *J. Pharm. Sci.* **2008**, *97*, 584–598.
- (47) Mitragotri, S.; Anissimov, Y. G.; Bunge, A. L.; Frasch, H. F.; Guy, R. H.; Hadgraft, J.; Kasting, G. B.; Lane, M. E.; Roberts, M. S. Mathematical models of skin permeability: An overview. *Int. J. Pharm.* **2011**, *418*, 115–129.
- (48) Frasch, H. F.; Barbero, A. M. Application of numerical methods for diffusion-based modeling of skin permeation. *Adv. Drug Delivery Rev.* **2013**, *65*, 208–220.
- (49) Wang, J.; Nitsche, J. M.; Kasting, G. B.; Wittum, G.; Nägel, A. Transdermal and lateral effective diffusivities for drug transport in stratum corneum from a microscopic anisotropic diffusion model. *Eur. J. Pharm. Biopharm.* **2023**, *188*, 271–286.
- (50) Lakey, P. S. J.; Eichler, C. M. A.; Wang, C.; Little, J. C.; Shiraiwa, M. Kinetic multi-layer model of film formation, growth, and chemistry (KM-FILM): Boundary layer processes, multi-layer adsorption, bulk diffusion, and heterogeneous reactions. *Indoor Air* **2021**, *31*, 2070–2083.

TOC Graphic



Supporting Information: Modeling Diffusion and Permeation Across the Stratum Corneum Lipid Barrier

Rinto Thomas^{†,¶}, Praveen Ranganath Prabhakar^{‡,¶}, Douglas J. Tobias[‡], and Michael von Domaros^{†,*}

[†]Fachbereich Chemie, Philipps-Universität Marburg, 35032 Marburg, Germany

[‡]Department of Chemistry, University of California, Irvine, Irvine, California, 92697 United States

[¶]R.T. and P.R.P. contributed equally to this work.

* mvondomaros@uni-marburg.de

S1 Impact of the Harmonic Force Constant on Diffusivity Profiles

A harmonic potential is required to restrain the solute at selected positions along the permeation path and to enable the VACF- and PACF-based analyses described in the main text. We employed three different force constants, $2.5 \text{ kcal mol}^{-1} \text{ \AA}^{-2}$, $30.0 \text{ kcal mol}^{-1} \text{ \AA}^{-2}$ and $50.0 \text{ kcal mol}^{-1} \text{ \AA}^{-2}$, which, in principle, should yield identical results. However, the strength of the restraint potential directly affects the behavior of both correlation functions, influencing their decay rates and corresponding Laplace spectra. Different force constants may therefore introduce numerical artifacts by altering the signal-to-noise ratio. A detailed discussion of these effects was provided by Rowley *et al.*¹

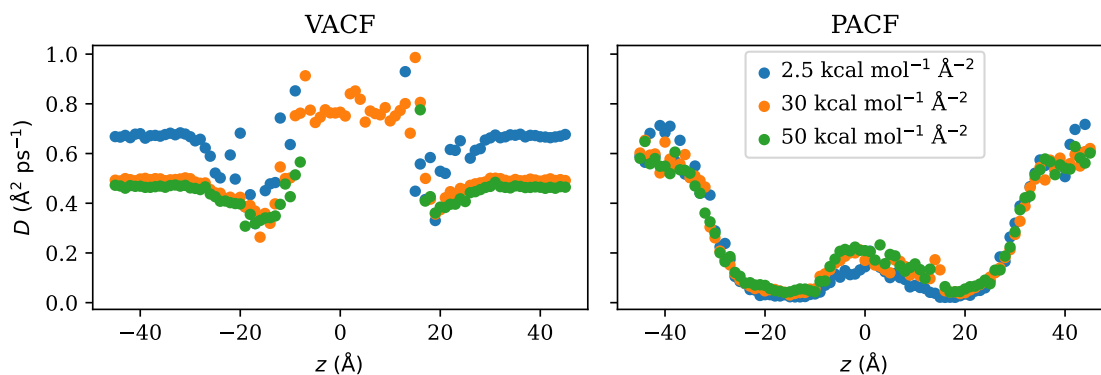


Figure S1: Diffusivity profiles of water obtained from the PACF and VACF analyses in the SC membrane at three different harmonic force constants.

Our results show similar trends, with modest variations in PACF-derived diffusivities across force constants but substantially larger variations in the VACF-derived values (Figure S1). In addition, some VACF-derived diffusivity profiles exhibit clear artifacts, likely stemming from limitations in the automated extrapolation procedure employed. We chose a force constant of $30 \text{ kcal mol}^{-1} \text{ \AA}^{-2}$ for the results presented in the main text, as this value produced the most stable and physically consistent profiles. Although more accurate VACF-based diffusivity profiles could, in principle, be obtained by carefully analyzing individual VACFs and their Laplace transforms and by manually tuning the extrapolation procedure, such an approach is laborious, error-prone, and potentially biased. These observations underscore the limited practicality of the VACF method.

S2 Bulk Diffusivities

To validate the diffusivity profiles presented in the main text, we calculated the diffusivities of all solutes in bulk water and compared them with those obtained at the center of the aqueous phase in our membrane system.

S2.1 Method

A single molecule of each solute and 2832 water molecules were placed in a rectangular simulation cell with dimensions of $57.15 \text{ \AA} \times 57.15 \text{ \AA} \times 26 \text{ \AA}$, resulting in a density of 1.00 g cm^{-3} for all systems, corresponding to the experimental density of water at a temperature of $T = 305.15 \text{ K}$ and a pressure of $P = 1 \text{ bar}$. The chosen box size approximately matches the size of the bulk water region in our membrane system. The systems were constructed using Packmol.²

Unless noted otherwise, the simulation parameters were consistent with those used in our previous work.³ Each system was first energy-minimized for 50 000 steps, followed by a short equilibration run of 1 ns in the NVT ensemble and a subsequent 20 ns simulation in the NPT ensemble. The system was then equilibrated for an additional 20 ns under NVT conditions prior to production runs. A total of 14 independent production trajectories of 1 ns each were performed, during which the center-of-mass coordinates of the solutes were recorded every 2 fs. Each 1 ns trajectory was subdivided into four 250 ps segments, yielding 56 segments per solute.

In homogeneous bulk systems, the Einstein relation connects the mean-squared displacement (MSD) to the diffusion coefficient D in the limit of long lag times t ,

$$\lim_{t \rightarrow \infty} \langle |\vec{r}(t) - \vec{r}(0)|^2 \rangle = 2dDt, \quad (\text{S1})$$

where \vec{r} denotes the center-of-mass position of the particle of interest, and d is the dimensionality of the system.

S2.2 Results and Discussion

Diffusion is inherently a size-dependent phenomenon,^{4,5} which is particularly important in the finite aqueous region of our membrane system. We therefore evaluated bulk diffusivities in a rectangular simulation cell of comparable size. In addition, we analyzed both one-dimensional ($d = 1$) diffusion along the z-axis of the simulation cell—most closely resembling the setup of the membrane system—and three-dimensional ($d = 3$) diffusion, which is the more common approach for studying bulk diffusion as it provides improved statistical sampling.

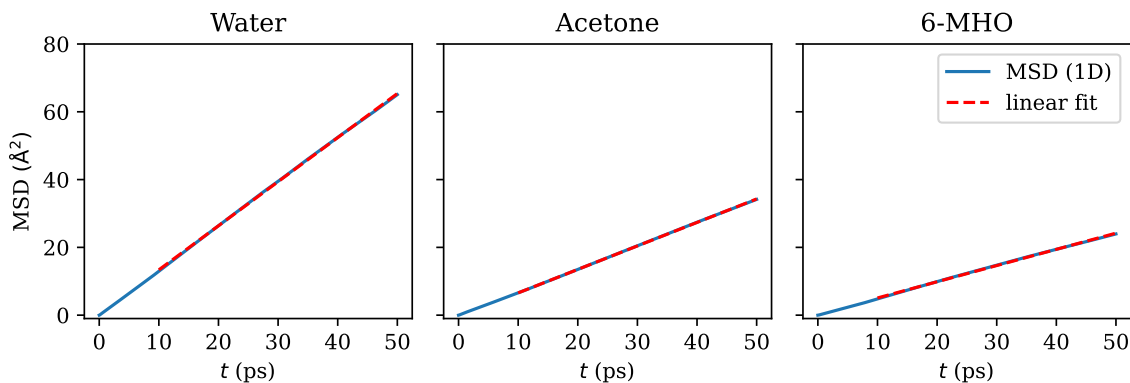


Figure S2: One-dimensional mean-squared displacements (MSDs) along the z-axis of the simulation cell for all solutes in bulk water.

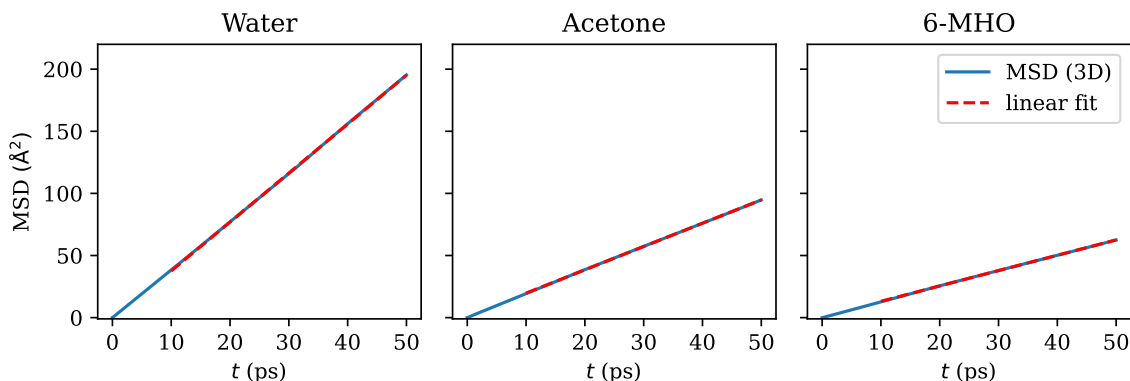


Figure S3: Three-dimensional mean-squared displacements (MSDs) for all solutes in bulk water.

Table S1: Bulk diffusion coefficients (in $\text{\AA}^2/\text{ps}$) for all solutes in bulk water, computed from the Einstein relation (eq. S1). Uncertainties represent the standard error of the mean across independent simulations and correspond to a 95% confidence interval.

Solute	1D	3D
Water	0.650 ± 0.109	0.657 ± 0.077
Acetone	0.346 ± 0.055	0.313 ± 0.033
6-MHO	0.239 ± 0.048	0.206 ± 0.021

Mean-squared displacements (MSDs) for the one-dimensional case are shown in Figure S2, and those for the three-dimensional case are presented in Figure S3. Bulk diffusivities, obtained from linear fits to the Einstein relation (eq. S1), are summarized in Table S1. For all fits, only lag times between 10 ps and 50 ps were considered.

Among the three solutes, the bulk diffusion coefficient is highest for water, followed by acetone and 6-MHO, consistent with the decrease in hydrodynamic radius across this series.

S3 Propagator Analysis

In Figure S4, we present the full set of propagators, $p(z, t | z_0 = 0, t_0 = 0)$, computed in the critical membrane-center region from both diffusion models for selected lag times t . The propagators were obtained using diffusivity profiles derived from the velocity autocorrelation function (VACF) and position autocorrelation function (PACF), in combination with the umbrella sampling (US) free-energy profiles shown in the main text. Between $t = 50$ ps and $t = 500$ ps, the results qualitatively match the representative example at $t = 100$ ps shown in the main text: neither the VACF- nor the PACF-based model reproduces the simulation data quantitatively. The VACF results consistently overestimate the diffusive spread, whereas the PACF results underestimate it.

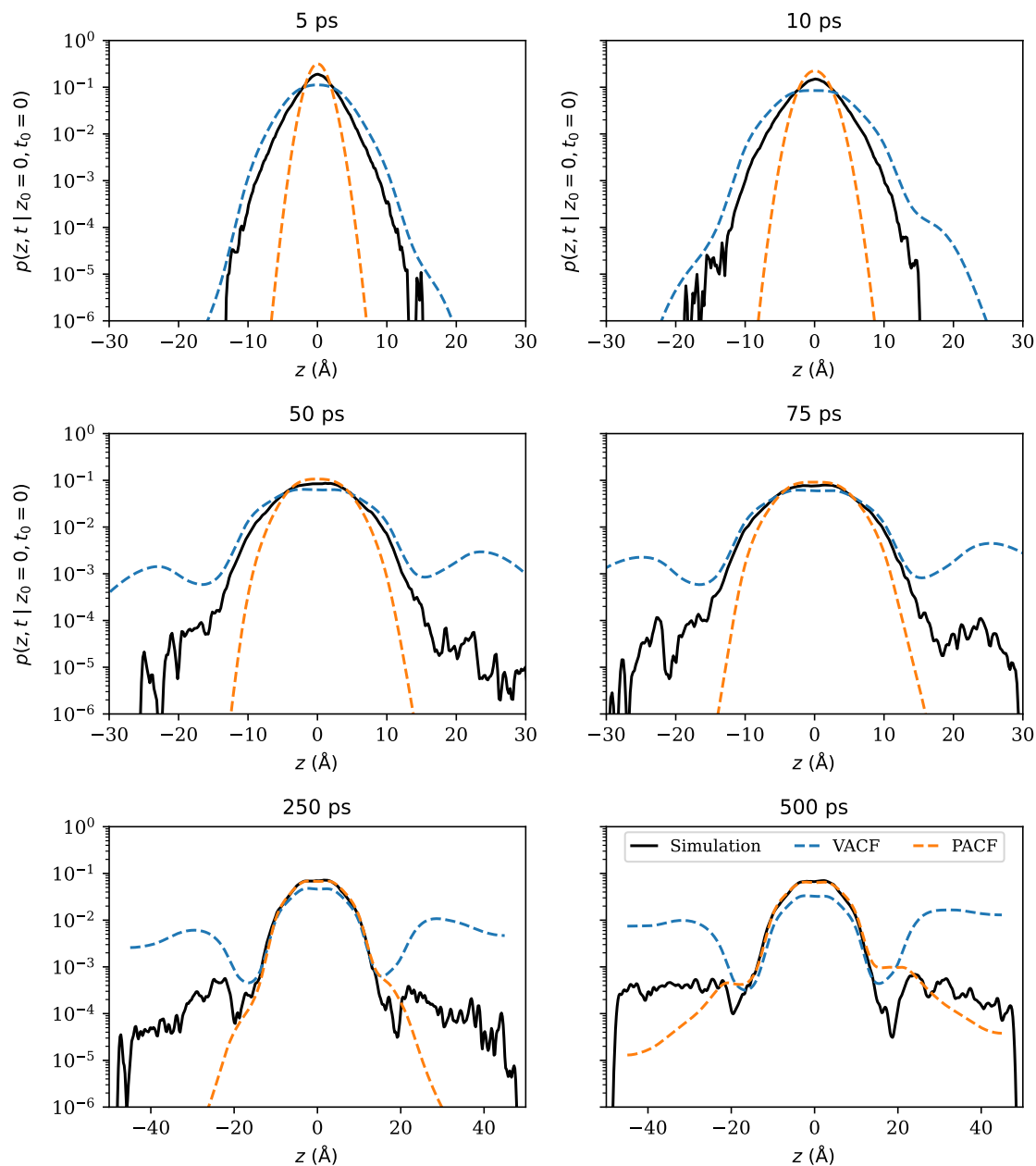


Figure S4: Propagators, $p(z, t | z_0, t_0)$, at different lag times ranging from $t = 5$ ps to $t = 500$ ps, obtained from simulations and diffusion models based on VACF- and PACF-derived diffusivity profiles combined with US free-energy profiles.

S4 Permeabilities

The estimation of membrane permeabilities using the inhomogeneous solubility–diffusion (ISD) model requires defining the membrane extent, h . Because of the soft and fluctuating

nature of lipid membranes, establishing precise boundaries is challenging. It is common practice to define the interfacial region based on the density profile, which is shown in Figure S5 for our SC model. However, there is no well-established criterion for selecting cutoff positions. In the absence of a standard definition, we considered three plausible choices for $h/2$: (i) the position where the water density begins to decrease from its bulk value ($h_1/2 = 32.0 \text{ \AA}$); (ii) the position where the water density is reduced to half of its bulk value ($h_2/2 = 25.5 \text{ \AA}$); and (iii) the position where the water density approaches zero ($h_3/2 = 17.0 \text{ \AA}$).

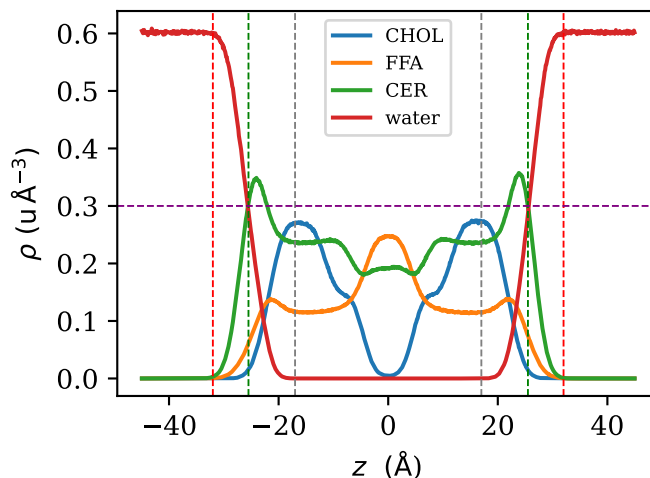


Figure S5: Component-wise density profile of the stratum corneum (SC) membrane (cholesterol, CHOL, blue; lignoceric acid, FFA, orange; ceramide NS, CER, green; and water, red). The red, green, and gray vertical dashed lines indicate the different integration limits tested at $h_1/2 = \pm 32.0 \text{ \AA}$, $h_2/2 = \pm 25.5 \text{ \AA}$, and $h_3/2 = \pm 17.0 \text{ \AA}$, respectively. The purple horizontal dashed line corresponds to half of the bulk water density.

Below we present the local resistance profiles, $R(z)$, for the combinations of free-energy and diffusivity methods not shown in the main text: US/PACF (Figure S6), WTM/VACF (Figure S7), and WTM/PACF (Figure S8). In all cases, the conclusion from the main text holds: the additional contribution to the area under the curve—and thus to the inverse permeability, P^{-1} —is negligible when changing from the smallest to the largest membrane extent considered. Any of the reasonable cutoff definitions therefore has little to no impact on the computed permeability.

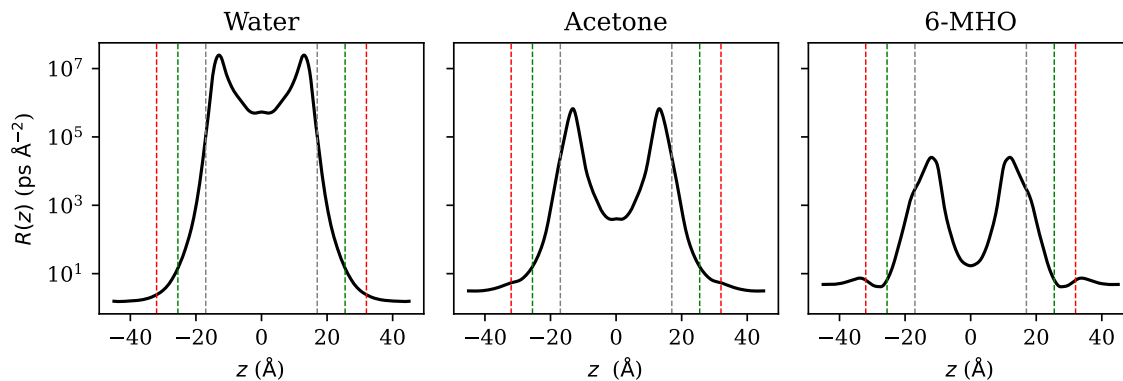


Figure S6: Local resistance, $R(z)$, estimated using the combination of umbrella sampling (US) free-energy profiles and PACF-derived diffusivities. Dashed vertical lines correspond to the different membrane extents defined in Figure S5.

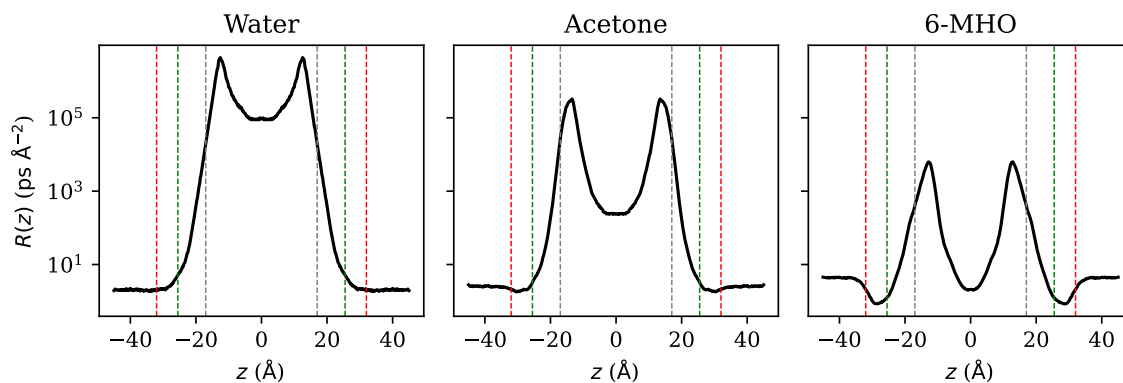


Figure S7: Local resistance, $R(z)$, estimated using the combination of well-tempered metadynamics (WTM) free-energy profiles and VACF-derived diffusivities. Dashed vertical lines correspond to the different membrane extents defined in Figure S5.

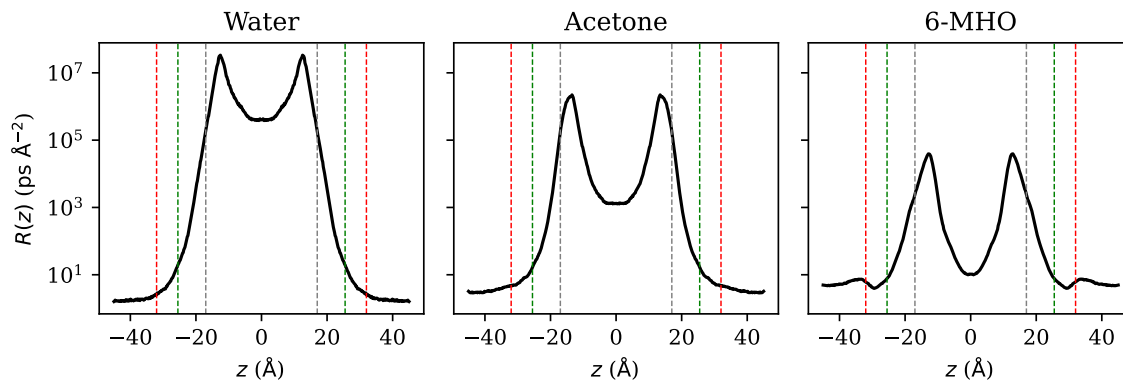


Figure S8: Local resistance, $R(z)$, estimated using the combination of well-tempered metadynamics (WTM) free-energy profiles and PACF-derived diffusivities. Dashed vertical lines correspond to the different membrane extents defined in Figure S5.

Finally, we present in Table S2 the numerical values of the membrane permeabilities that are plotted graphically in the main text.

Table S2: Membrane permeabilities (in cm s^{-1}) calculated using position autocorrelation function (PACF) and velocity autocorrelation function (VACF) methods. Free-energy profiles were obtained from umbrella sampling (US) and well-tempered metadynamics (WTM). The corresponding bar plots are shown in the main text.

Solute	PACF		VACF	
	US	WTM	US	WTM
Water	5.65×10^{-5}	5.48×10^{-5}	4.15×10^{-4}	4.00×10^{-4}
Acetone	2.60×10^{-3}	7.48×10^{-4}	1.75×10^{-2}	5.04×10^{-3}
6-MHO	4.55×10^{-2}	4.18×10^{-2}	2.82×10^{-1}	2.60×10^{-1}

References

- [1] Gaalswyk, K.; Awoonor-Williams, E.; Rowley, C. N. Generalized Langevin methods for calculating transmembrane diffusivity. *J. Chem. Theory Comput.* **2016**, *12*, 5609–5619.
- [2] Martínez, L.; Andrade, R.; Birgin, E. G.; Martínez, J. M. PACKMOL: A package for building initial configurations for molecular dynamics simulations. *J. Comput. Chem.* **2009**, *30*, 2157–2164.
- [3] Thomas, R.; Prabhakar, P. R.; Tobias, D. J.; von Domaros, M. Insights into dermal permeation of skin oil oxidation products from enhanced sampling molecular dynamics simulation. *J. Phys. Chem. B* **2025**, *129*, 1784–1794.

- [4] Yeh, I.-C.; Hummer, G. System-Size Dependence of Diffusion Coefficients and Viscosities from Molecular Dynamics Simulations with Periodic Boundary Conditions. *J. Phys. Chem. B* **2004**, *108*, 15873–15879.
- [5] Jamali, S. H.; Wolff, L.; Becker, T. M.; Bardow, A.; Vlugt, T. J. H.; Moulton, O. A. Finite-size effects of binary mutual diffusion coefficients from molecular dynamics. *J. Chem. Theory Comput.* **2018**, *14*, 2667–2677.